Supporting Information

Electrolyte Driven Highly Selective CO_2 Electroreduction at Low Overpotentials

Tengfei Li,[a,b] Chao Yang,[a] Jing-Li Luo,[b,*] Gengfeng Zheng[a,*]

[a] Laboratory of Advanced Materials, Department of Chemistry and Shanghai Key Laboratory of Molecular Catalysis and Innovative Materials, Fudan University, Shanghai 200438, China

[b] Department of Chemical and Materials Engineering, University of Alberta, Edmonton, Alberta T6G 1H9, Canada

* Corresponding authors:

Prof. Jing-Li Luo (E-mail: jingli.luo@ualberta.ca)

Prof. Gengfeng Zheng (E-mail: gfzheng@fudan.edu.cn)

Table of Contents

1. Experimental section

1.1. Electrocatalyst synthesis

Copper(II) sulfate pentahydrate ($CuSO_4 \cdot 5H_2O$, 99+%, ACROS Organics), sodium hydroxide (NaOH, 97%, Fisher Chemical), L-Ascorbic Acid (AA, 99%, Fisher Chemical) and Tin(IV) chloride pentahydrate ($SnCl_4 \cdot 5H_2O$, 98+%, ACROS Organics) were used without further purification. In a typical procedure, 90 mL of deionized water was introduced into a 200-mL beaker. Subsequently, 1 mL of 0.1 M $CuSO_4$ solution was added to the beaker. The beaker was kept in a water bath at 35 ℃ throughout the synthesis. Next, 4.75 mL of 1.0 M NaOH solution was introduced into the beaker with vigorous stirring. Then, it was observed that the solution turned light blue immediately, indicating the formation of $Cu(OH)_2$ precipitate. With the addition of 5 mL of 0.2 M AA solution, the above solution turned to orange-yellow from light green gradually. The solution was stirred for 10 min for Cu_2O crystal growth in the water bath. And then Cu_2O nanocubes were collected by suction filtration and washed with deionized water and ethanol thoroughly to remove residual ions and dried in a vacuum oven at 60℃ for 12 hours for further use. The core-shell structured $Cu_2O@SnO_x$ nanoparticles were synthesized by dropwise adding 1.75 mL of an ethanol solution of $SnCl_4$ (1 mM) into a suspension of 0.035 mmol of the as-prepared Cu_2O nanocubes in 10 mL of ethanol and 0.3 mL of aqueous NaCl solution (1.71 M) under stirring at room temperature for 10 min. The as-obtained products were collected by suction filtration and washed with deionized water and ethanol thoroughly to remove residual ions and dried in a vacuum oven at 60℃ for 12 hours for further characterization.

1.2. Structural characterizations

The crystalline structure of the samples was characterized by X-ray diffraction (XRD) analysis with a Rigaku XRD Ultima IV diffractometer using Cu Kα radiation generated at 40 kV and 44 mA. The XRD pattern was recorded within a 2θ range from 20 to 80 at 2° min^{-1}. The morphology of the materials was imaged using a Zeiss Sigma Field Emission SEM. The composition was analyzed with an Orbis PC Micro-XRF Analyzer. Transmission electron microscope analysis, scanning transmission electron microscopy (STEM) energy-dispersive X-ray spectroscopy (EDS) were performed using a JEOL JEM-ARM200CF Atomic Resolution S/TEM. X-ray photoelectron spectroscopy (XPS, Kratos AXIS) was carried out to examine the surface chemistry of the sample.

1.3. Electrochemical measurements

To prepare the working electrode, a suspension with a proportion of 15 mg of powders (10 mg of electrocatalysts and 5 mg of carbon black), 0.76 mL of ethanol, 1.14 mL of DI water, and 100 μL of 5 wt.% Nafion solution was sonicated to achieve a homogeneous dispersion. The resulting suspension was then painted onto one side of a Toray carbon paper (1 cm × 2 cm, Toray TGP-H-060, Toray Industries Inc.) to achieve an electrocatalyst loading of 1 mg cm^{-2}. All the potentials were recorded against the reference electrode and converted to the reversible hydrogen electrode (RHE) reference scale by the equation, $E_{RHE} = E_{SCE} + 0.241 + 0.0591 \times pH$. The pH values of CO_2-

saturated 0.1, 0.3, 0.5, and 0.7 M $KHCO_3$ were 6.8, 7.2, 7.5, and 7.6, respectively. The Current densities in this work were all normalized to the geometric surface area.

All the experiments were carried out on a potentiostat/galvanostat (Autolab PGSTAT302N) in a two-compartment gastight H-cell separated by a Nafion membrane (Nafion® 117, Alfa Aesar) with a saturated calomel electrode (SCE) reference electrode and a piece of platinum gauze (3 cm × 3 cm) counter electrode. Each compartment contained 39 mL of electrolyte and left a headspace of about 31 mL. The $KHCO_3$ aqueous solution was used as electrolyte directly without any purification. Prior to the CO_2 reduction, the cathodic electrolyte was saturated with CO_2 (99.99%, Praxair Canada Inc.) at a flow rate of 20.0 mL min^{-1} controlled by a mass flow controller (Brooks Instrument). In order to enhance the mass transport of CO_2, the catholyte was magnetically stirred during the electrolysis. The gas products of CO_2 electroreduction from the cathode compartment were analyzed using an on-line gas chromatography (GC, Agilent 6890N) equipped with a flame ionization detector (FID) and a thermal conductivity detector (TCD). The FID with methanizer was used to quantify CO, CH_4, C_2H_4, and C_2H_6, and the TCD was used to quantify H_2. A standard gas mixture composed of CH_4, C_2H_4, C_2H_6, CO, H_2, and CO_2 (Praxair Canada Inc.) was applied to obtain the calibration curve for each component. Argon was employed as the carrier gas. Every GC run lasted for 8.4 min. For every potential, the first GC run was initiated at the 10^{th} min, and thereafter reinitiated every 8.4 min for twice. The average of the results from these three measurements was used in the data analysis.

1.4. Calculation of energetic efficiency (EE)

Cathodic voltage efficiency: $VE_{cathodic} = \frac{1.23 + (-E_{CO})}{1.23 + (-E_{cathode})}$ (S1)

CO cathodic energetic efficiency: $EE_{cathodic} = VE_{cathodic} \times FE_{CO}$ (S2)

where $E_{cathode}$ was the applied cathode potential versus RHE; E_{CO} = –0.11 V versus RHE was the thermodynamic potential of CO_2 reduction to CO; FE_{CO} was the Faradaic efficiency toward CO.

1.5. Synergistic effect between Cu and Sn

The observed enhanced selectivity for CO on the Sn-OD-Cu was attributed to the synergistic effect between Cu and Sn. To interpret the synergistic reaction mechanism, the electronic structure of the hybrid catalyst surface must be taken into consideration. It could be modified by the electron relocation between Cu and Sn, which altered its binging strength for reaction intermediates.

The *d*-band center was one of the most widely-used reactivity descriptors for the chemisorption models on transition-metal surfaces and their alloys.[1] Generally, a metal site with a higher *d*-band center exhibited a stronger affinity to adsorbates.[2]

The combination of Cu with Sn caused the charge transfer from Sn to Cu because Cu had a stronger electronegativity than Sn,[3] and a half-empty 4s band that could act as an electron acceptor.[4] In this work, the positively chemical shift measured by XPS for Sn 3d confirmed the electron transfer from Sn to Cu which was consistent with the previous report.[5] In addition, a Bader analysis also indicated the charge transfer from

Sn to Cu in a Cu-Sn alloy.[6] Such charge transfer would result in an up-shift of the *d*-band center of surface Cu sites which could strengthen the substrate-adsorbate interaction.

The activation of CO_2 through the formation of a *COOH intermediate on Cu sites generally had an uphill energy barrier.[7] The enhanced affinity of the Cu site to *COOH intermediate due to the upshifted *d*-band center significantly decreased the energy barrier for the formation of *COOH intermediate.

In addition to the desirable electronic structure, the favorable adsorption geometry was also important. Sn was identified as a metal with higher O affinity and weaker H affinity than Cu.[8] The additional O-Sn binding contributed by the O-binding site of Sn added up to the stability of *COOH on the Cu sites. In this work, the first proton-coupled electron-transfer step to form the *COOH intermediate was proposed as the rate-determining step. Thus, the improved *COOH stability resulted in a lowered energy barrier for CO_2 reduction to CO on the Cu-Sn hybrid catalyst. Therefore, the origin of the improved selectivity of the Sn-OD-Cu for CO came from a combination of electronic and geometric effects.

Furthermore, through the density functional theory calculations, the above-mentioned combined effect weakened the binding of *H intermediate of Cu-Sn hybrid catalyst which increased the thermodynamic limiting potential for H_2 production.[6]

The Cu/SnO interface was supposed to play an indispensable role in the combined effect. However, the complete covering of Cu with SnO was unlikely to support the combined effect (Figure S5).

1.6. iR-correction

A current interrupt measurement was performed to determine the uncompensated resistance value (R_u). As illustrated in Table S2, R_u was measured at different potentials in CO_2-saturated $KHCO_3$ solution with different concentrations. R_u varied little with the potential, but, decreased as the concentration of $KHCO_3$ increased.

Then, the potentials used for plotting were corrected by using the measured R_u (Table S3). The magnitude of potential correction increased as the potentials became negatively. With iR-correction, the potential became positively with a maximum percentage change of 23.4% in 0.1 M CO_2-saturated $KHCO_3$ solution as compared with the initially used potential of –1.2 V versus RHE. However, over the low- to the moderate-overpotential range (< –0.7 V versus RHE), the correction was less than 10%. As the differences between potentials with and without iR-correction over the low-overpotential range were very little, the electrokinetic analysis, including the Tafel plot analysis and reaction order study over the kinetically controlled region (i.e., low-overpotential range), was consistent at potentials with and without iR-correction. Based on the above discussion, the ohmic drop plays a negligible effect on the electrokinetic analysis. In other words, the observed enhancement on the activity of CO_2RR was really an effect of the concentration of HCO_3^-.

As such, Figure 4a in the main text was replotted using the iR-corrected potentials. With iR-correction, the Sn-OD-Cu exhibited better performance, including the maximum CO partial current density of 25.0 mA cm^{-2} at a lowered overpotential in 0.7 M CO_2-saturated $KHCO_3$ solution (Figure S17). To facilitate the comparison with other

reported results, as well as the reaction order study conducted at the consistent potential in CO_2-saturated $KHCO_3$ solution with different concentrations, the potentials without iR-correction were applied in this work.

1.7. Derivation of the theoretical Tafel slope and reaction order with respect to $[HCO_3^-]$

The first electron transfer for the formation of $CO_2^{\cdot-}$ was regarded as the rate-determining step (RDS) in the electrochemical reduction of CO_2 to CO when a Tafel slope of ~118 mV dec^{-1} was obtained. However, it was incomprehensible that the formation of $CO_2^{\cdot-}$ (–1.9 V versus SHE) was much more negative than the onset potential for CO production.[9]

Except for the formation process of $CO_2^{\cdot-}$ regarded as the activation step for CO_2, the formation process of the intermediate of *COOH by a proton-coupled electron transfer (PCET) was also considered to be the CO_2 activation step.[10-20]

Based on the proposed RDS ($CO_2 + HCO_3^- + e^- + * \rightarrow COOH^* + CO_3^{2-}$), the CO partial current could be described as

$$i_{CO} = nFk[CO_2][HCO_3^-](1-\theta)\exp(\frac{-\beta EF}{RT}) \quad (S3)$$

where θ was the total surface coverage, E was the applied potential, k was a rate constant for the RDS, β was the symmetry factor and was assumed to be equal to 0.5, F was Faraday's constant, R was the gas constant, and T was the temperature. The derived value of the Tafel slope was $2.3RT/\beta F$, or 118 mV dec^{-1}, which was consistent with the

experimental obtained Tafel slope values.

Based on the rate expression of Eq. S3, the partial derivative of the j_{CO} with respect to [HCO_3^-] or [CO_2] at constant overpotentials yielded an expression for the reaction order equaling to 1, as shown below:

$$\log(i_{CO}) = \log(nFk(1-\theta)) + \log([CO_2]) + \log([HCO_3^-]) + \frac{-\beta EF}{2.3RT} \quad (S4)$$

$$\frac{\partial \log(i_{CO})}{\partial \log([CO_2])} = 1 \quad (S5)$$

$$\frac{\partial \log(i_{CO})}{\partial \log([HCO_3^-])} = 1 \quad (S6)$$

The kinetic modeling of the CO_2 bubbling showed that [CO_2] maintained constant in CO_2-saturated $KHCO_3$ solution with different concentrations. Therefore, it could be concluded that the experimentally obtained reaction order with respect to [HCO_3^-] was independent with [CO_2] and consistent with the theoretically calculated one in the kinetically controlled region (i.e., low overpotential range).

1.8. Concentration effect of $KHCO_3$ on the activity of H_2 and C_2H_4 production

In the main text, the concentration effect of $KHCO_3$ on the activity for CO_2 conversion to CO was kinetically analyzed from reaction order study. Using the same method, the concentration effect of $KHCO_3$ on the activity for H_2 and C_2H_4 production was also studied. The linear correlation was also found between log (j_{H2} or j_{C2H4}) and log ([HCO_3^-]) (Figure S18). The slopes of the plots of log (j_{CO} or j_{H2} or j_{C2H4}) versus log ([HCO_3^-]) at the different potentials were listed in Table S4. The positive and negative values of the slopes indicated the promoting and inhibiting effects respectively.

The magnitude of the numerical absolute value of a slope indicated the degree of the effect.

For CO_2RR to CO, the slopes decreased as the potentials became more negative, indicating that the promotion effect of $KHCO_3$ concentration on CO production weakened as the potentials became more negative. For the HER, there was a role transition for $KHCO_3$ concentration effect as the potentials became more negative, which initially suppressed HER and then promoted it. For CO_2RR to C_2H_4, the promotion effect of $KHCO_3$ concentration increased as the potentials became more negative.

Because of the different modes of action of the concentration effect of $KHCO_3$ on different reactions, the relative activities of the catalyst to different products maintained almost constant when the concentration of $KHCO_3$ increased from 0.3 M to 0.7 M. The almost unchanged relative activities resulted in the similar FEs in 0.3 ~ 0.7 M $KHCO_3$.

2. Supplementary Figures (Figure S1–S18)

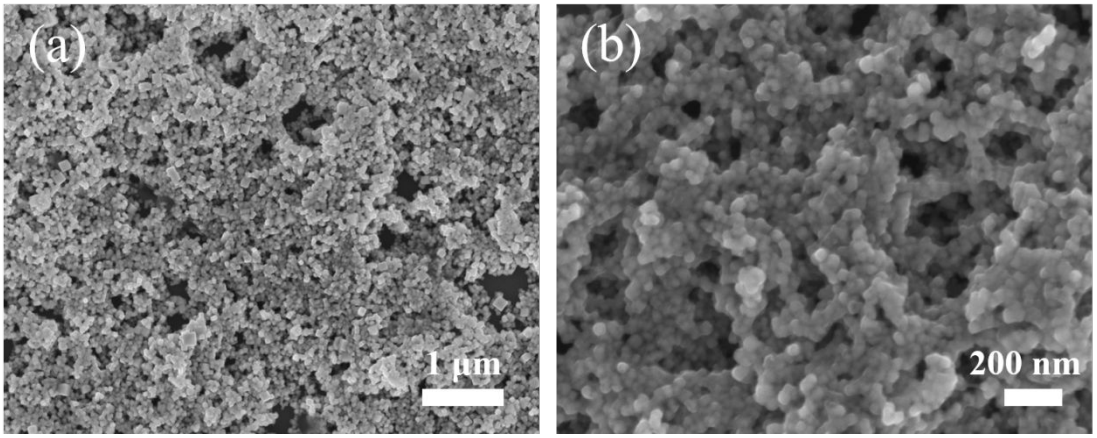

Figure S1. SEM images of (a) Cu_2O nanocubes and (b) SnO_x modified Cu_2O.

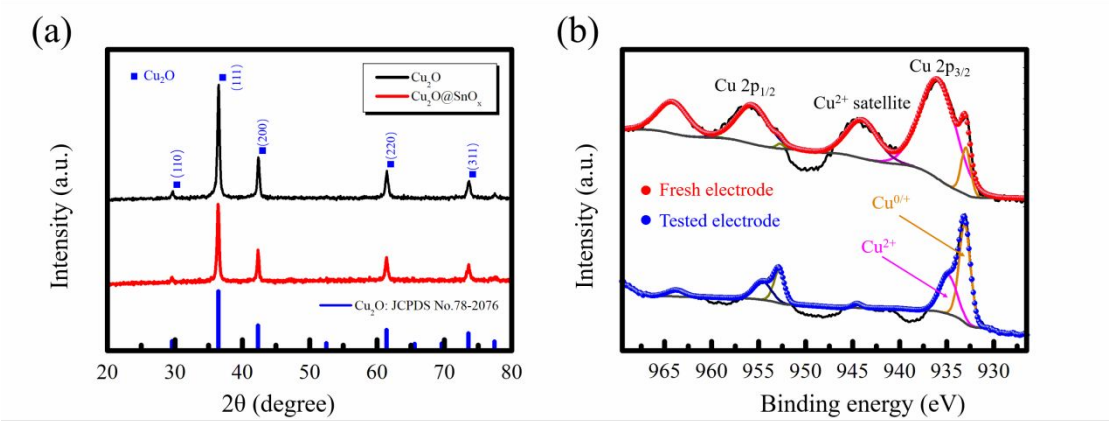

Figure S2. (a) X-ray diffraction pattern of as-prepared Cu_2O and $Cu_2O@SnO_x$ core-shell nanoparticles. (b) Cu 2p XPS spectrum and the corresponding fitting results of the fresh and tested electrodes of $Cu_2O@SnO_x$ core-shell nanoparticles.

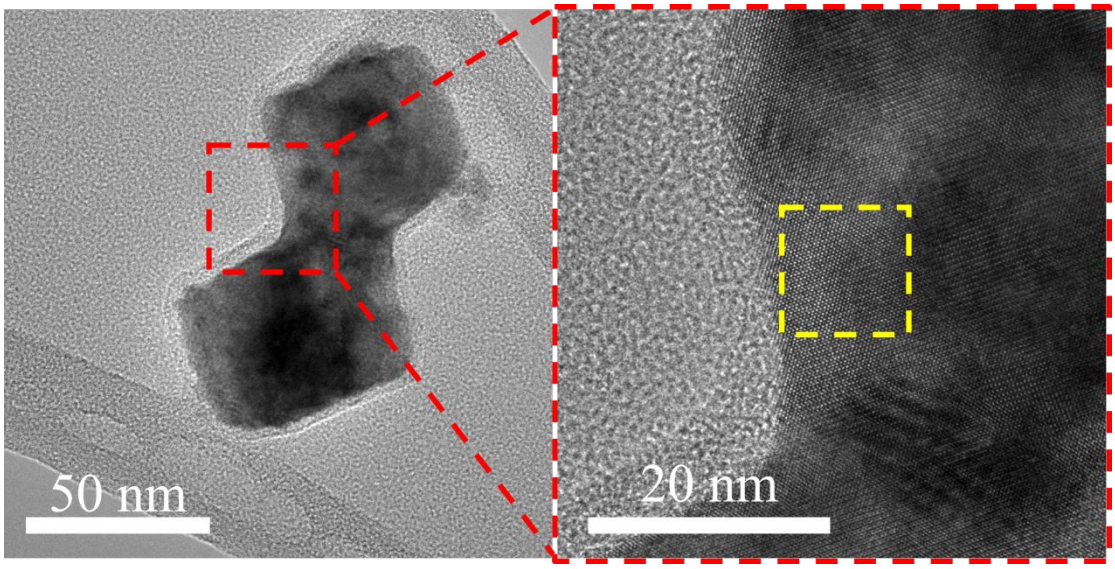

Figure S3. The high-resolution TEM image of SnO_x modified Cu_2O.

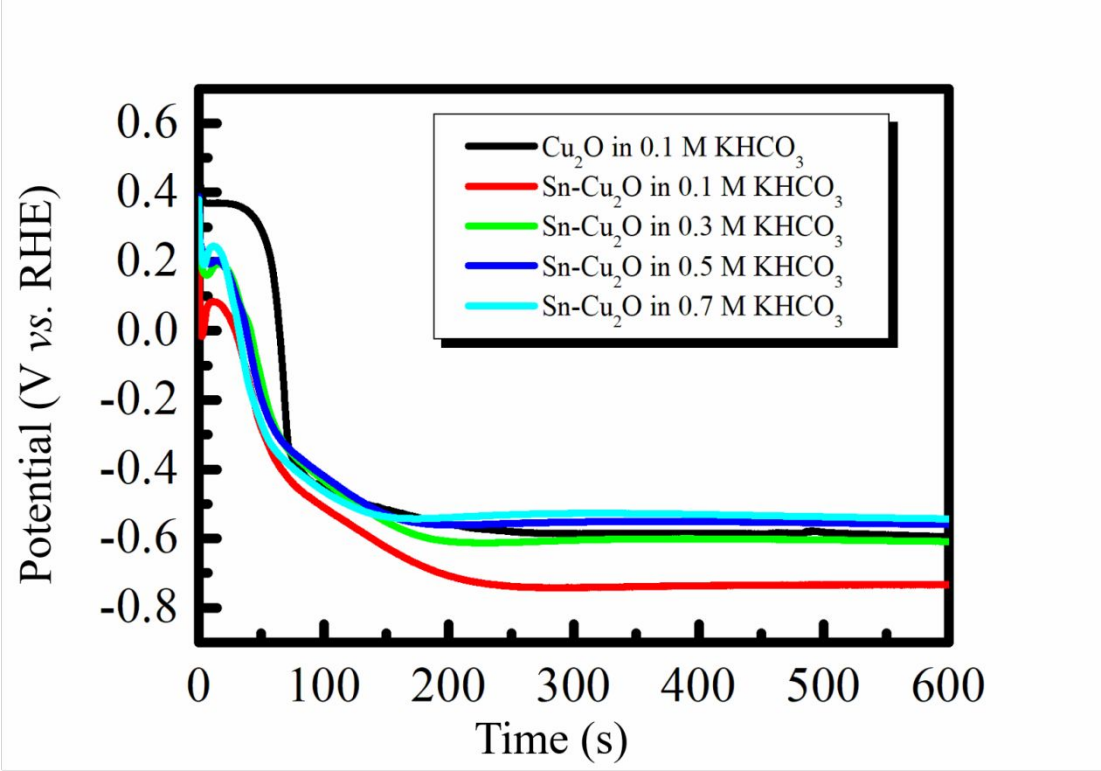

Figure S4. Potential versus time recorded during reduction at –3.0 mA cm^{-2} of Cu_2O in CO_2-saturated 0.1 M $KHCO_3$ solution and of SnO_x modified Cu_2O in CO_2-saturated $KHCO_3$ solution with different concentrations.

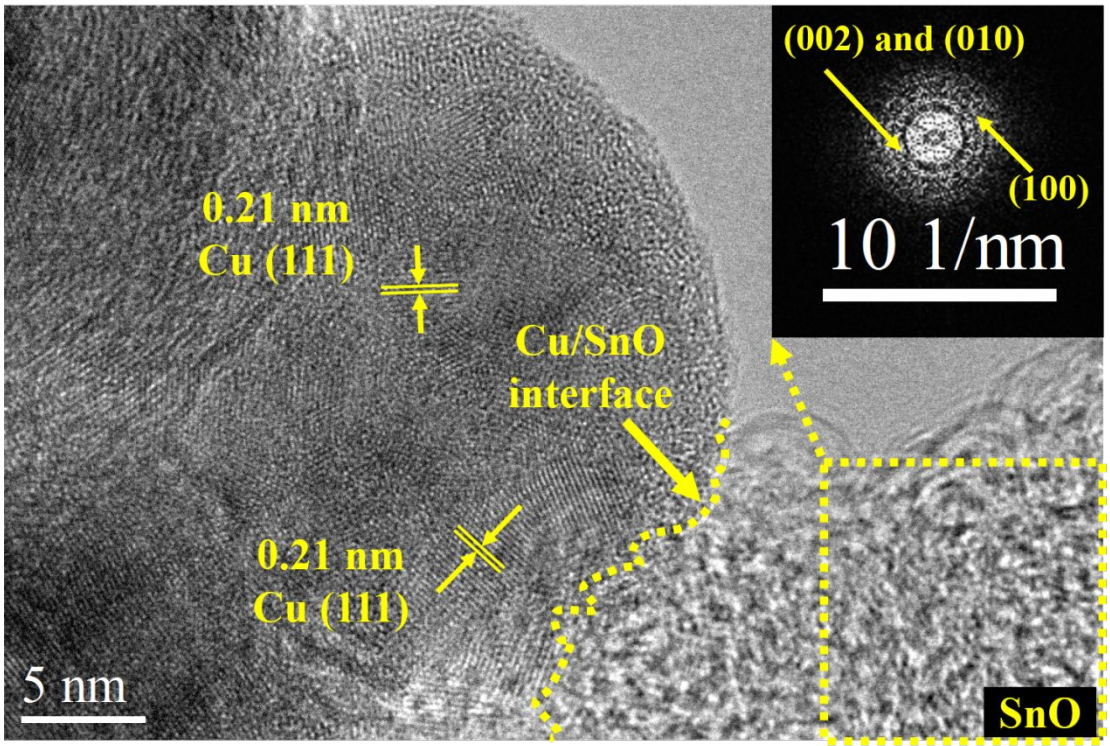

Figure S5. High-resolution TEM image and the corresponding fast Fourier transformation image of the core-shell structured $Cu_2O@SnO_x$ nanoparticle derived hybrid catalyst in the tested electrode.

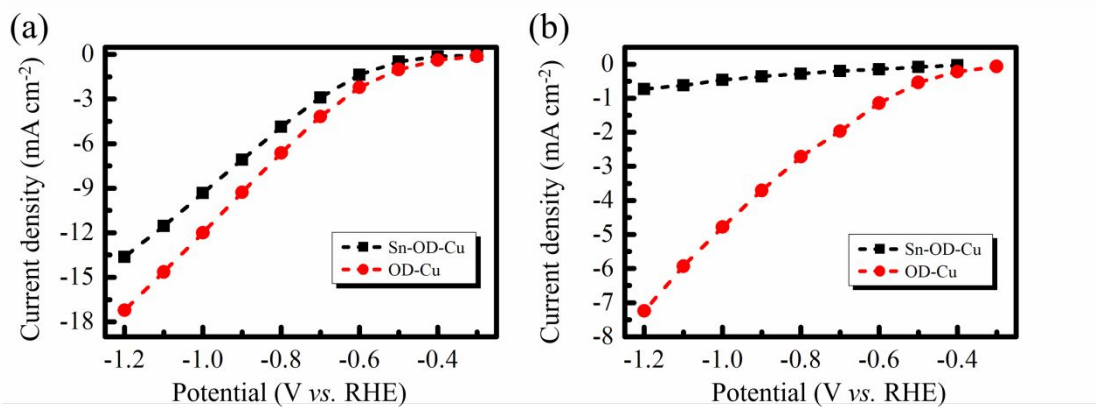

Figure S6. (a) Total current densities and (b) partial current densities of H_2 on Sn-OD-Cu and OD-Cu in CO_2-saturated 0.1 M $KHCO_3$ solution at various potentials.

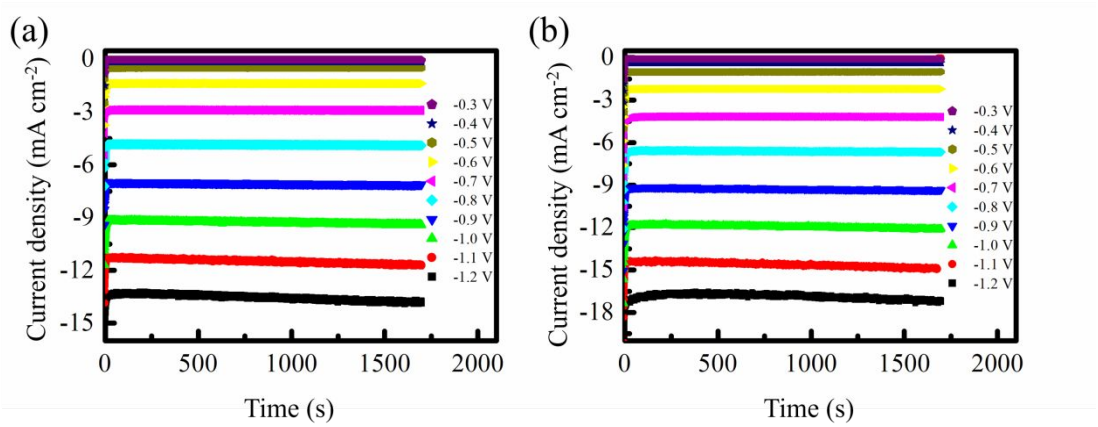

Figure S7. Current densities as a function of time at various applied potentials for CO_2 reduction experiments on (a) Sn-OD-Cu and (b) OD-Cu in CO_2-saturated 0.1 M $KHCO_3$ solution.

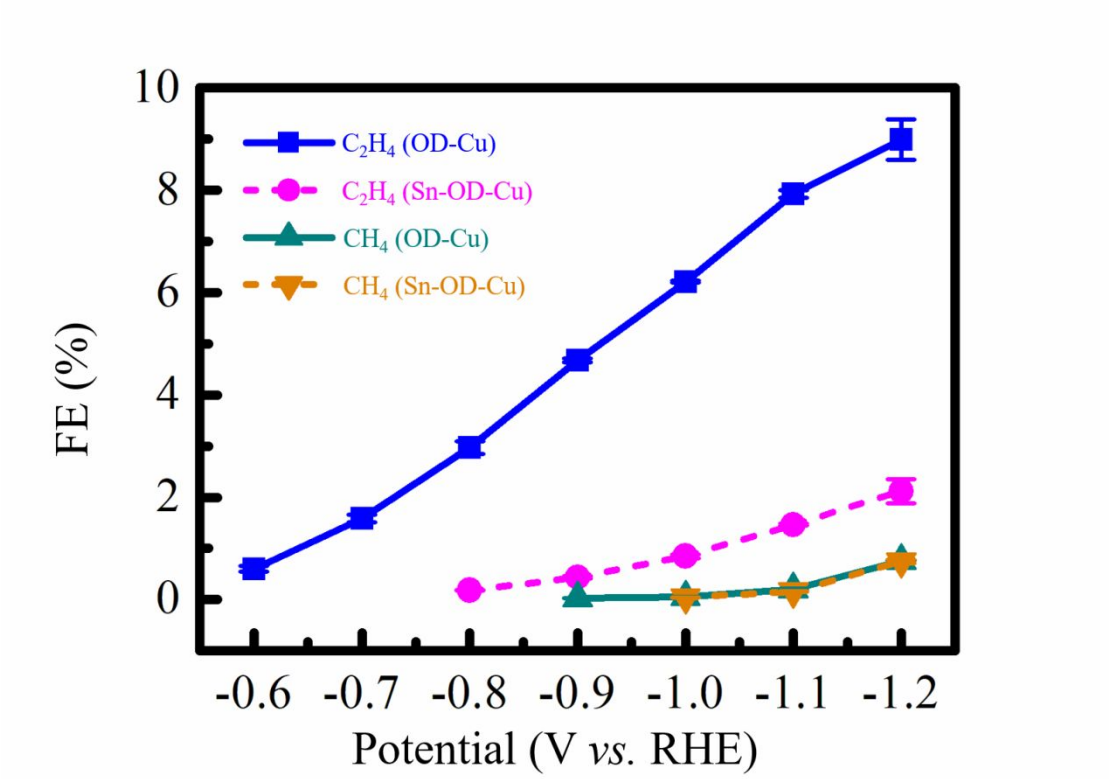

Figure S8. FEs of hydrocarbon products over the Sn-OD-Cu and OD-Cu at various potentials.

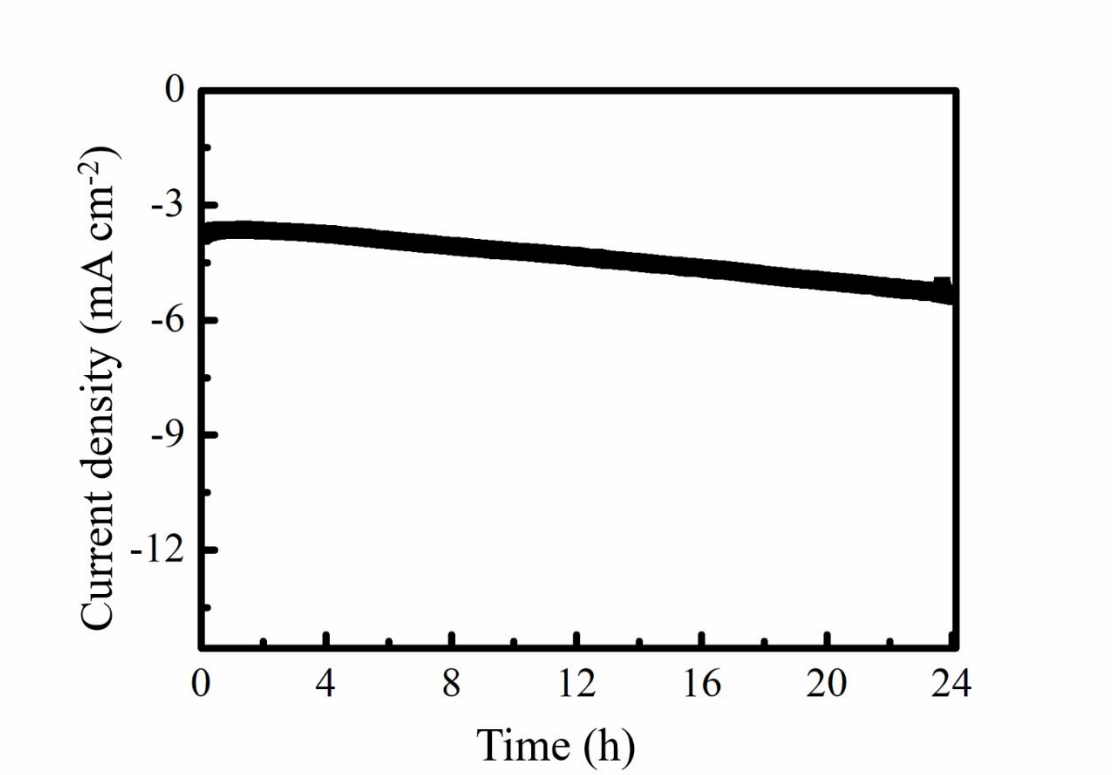

Figure S9. Total current density versus time at –0.8 V versus RHE during the long-term stability test for 24 h of Sn-OD-Cu in CO_2-saturated 0.1 M $KHCO_3$.

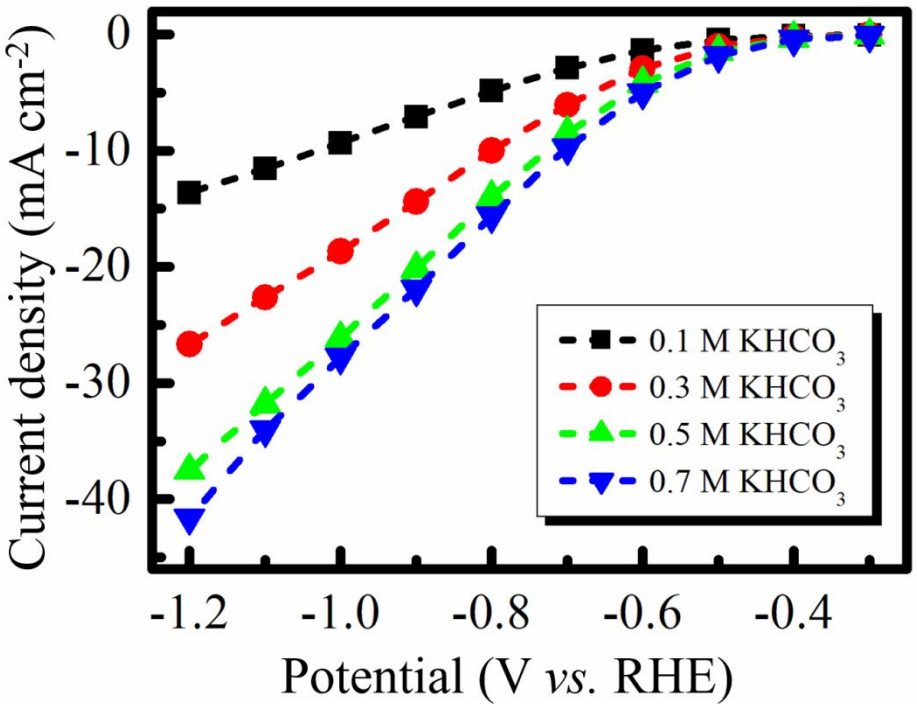

Figure S10. Total current densities on Sn-OD-Cu derived from chrono-amperometric measurements in CO_2-saturated $KHCO_3$ solution with different concentrations.

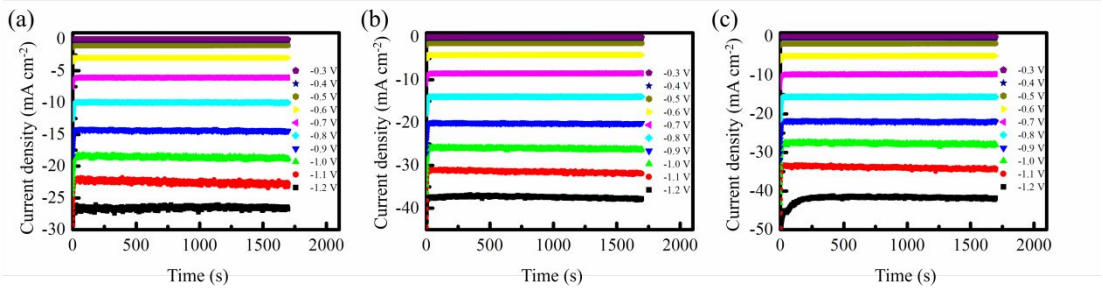

Figure S11. (a-c) Current density as a function of time at various applied potentials for CO_2 reduction experiments on Sn-OD-Cu in CO_2-saturated 0.3, 0.5 and 0.7 M $KHCO_3$ solution, respectively.

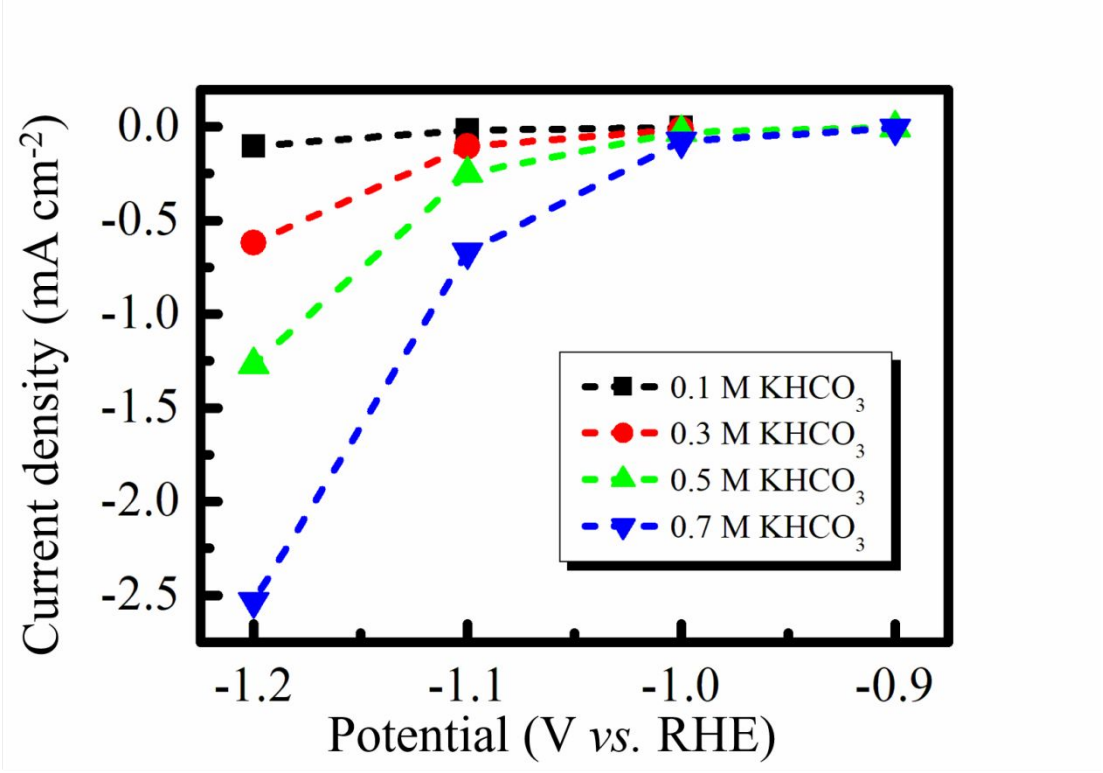

Figure S12. Partial current densities of CH_4 on Sn-OD-Cu derived from chrono-amperometric measurements in CO_2-saturated $KHCO_3$ solution with different concentrations.

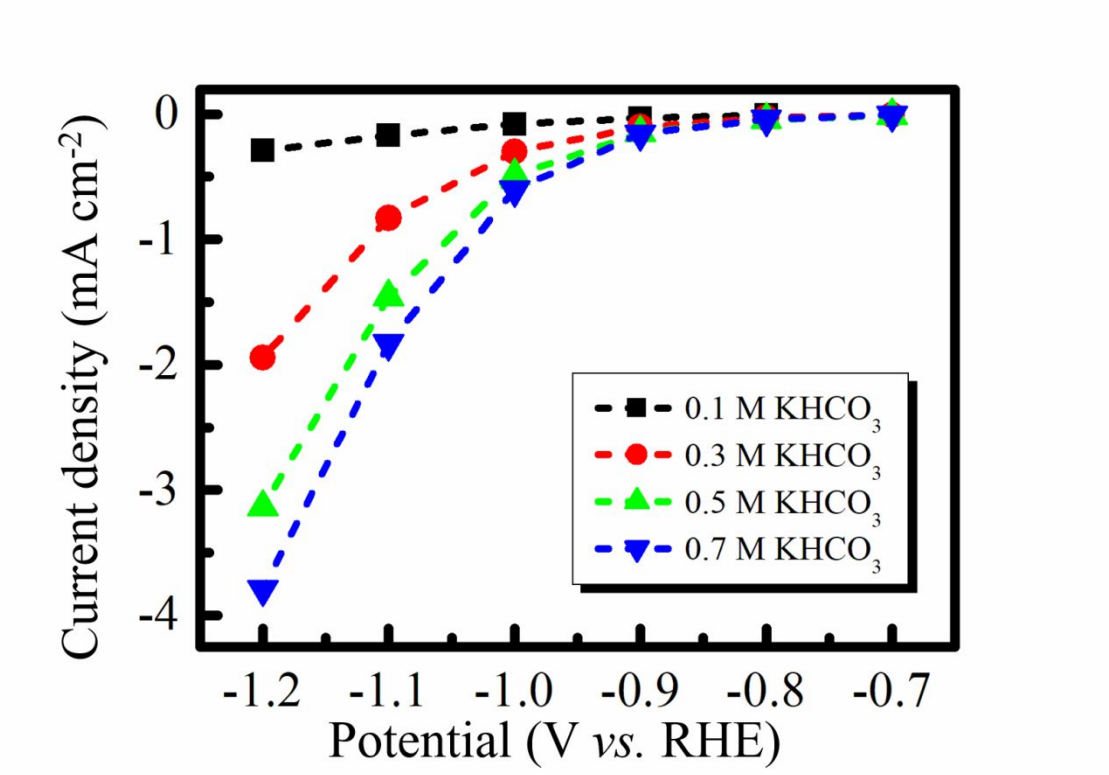

Figure S13. Partial current densities of C_2H_4 on Sn-OD-Cu derived from chrono-amperometric measurements in CO_2-saturated $KHCO_3$ solution with different concentrations.

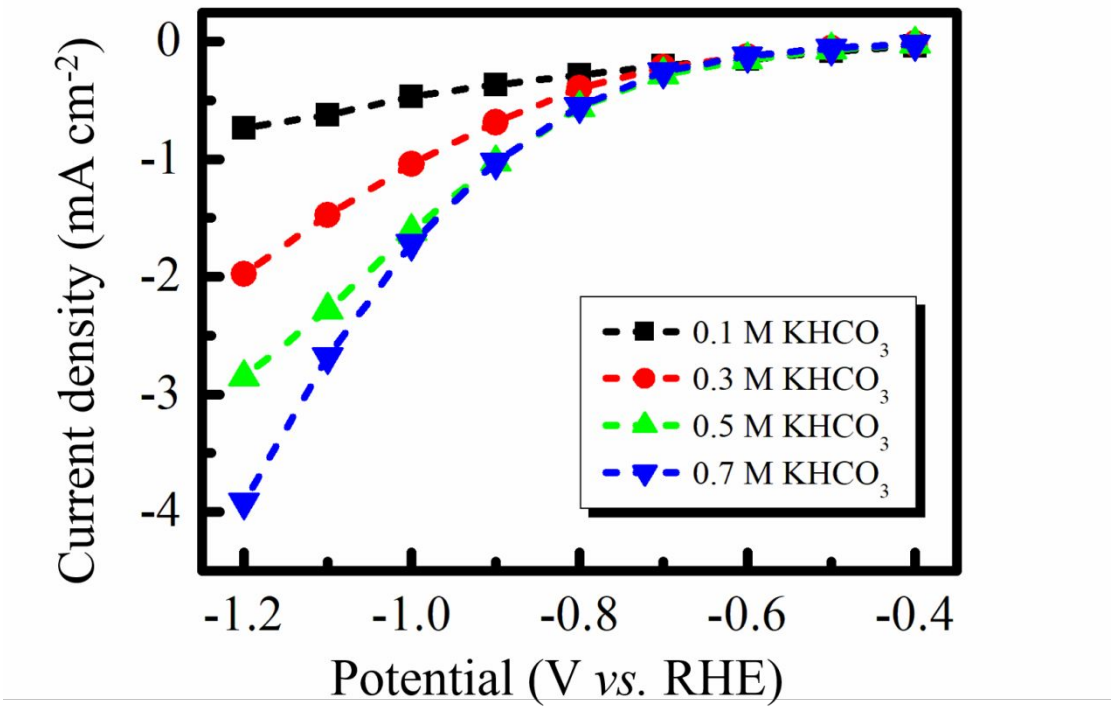

Figure S14. Partial current densities of H_2 on Sn-OD-Cu derived from chrono-amperometric measurements in CO_2-saturated $KHCO_3$ solution with different concentrations.

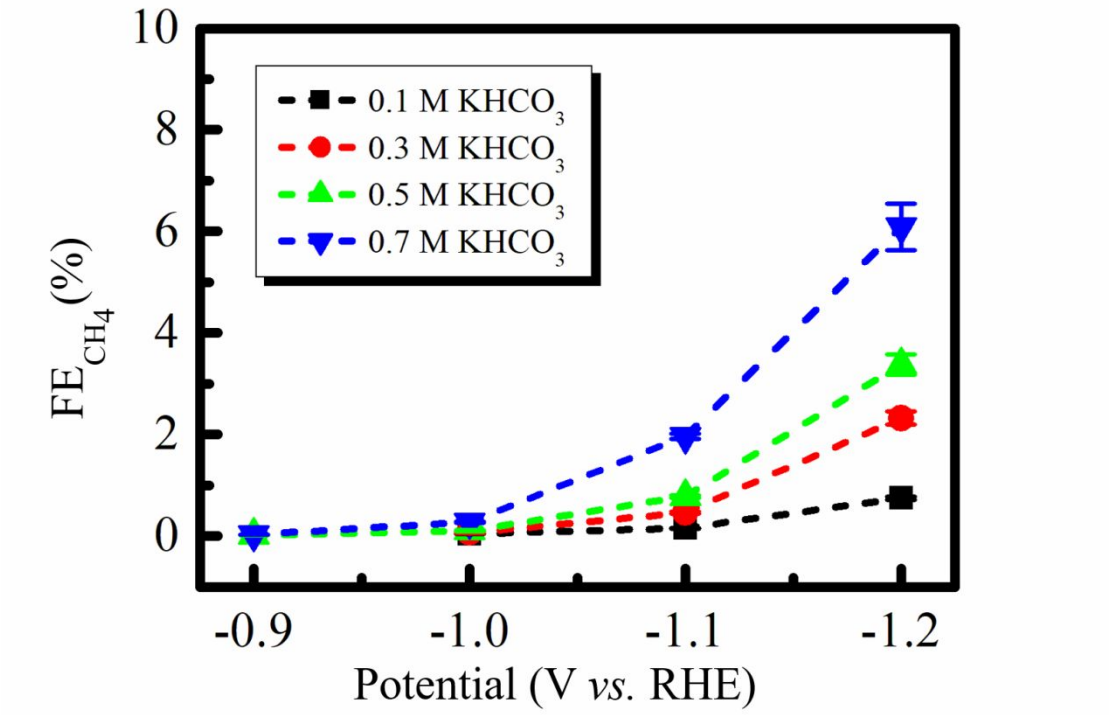

Figure S15. Faradaic efficiencies of CH_4 at different potentials for Sn-OD-Cu in CO_2-saturated $KHCO_3$ solution with different concentrations

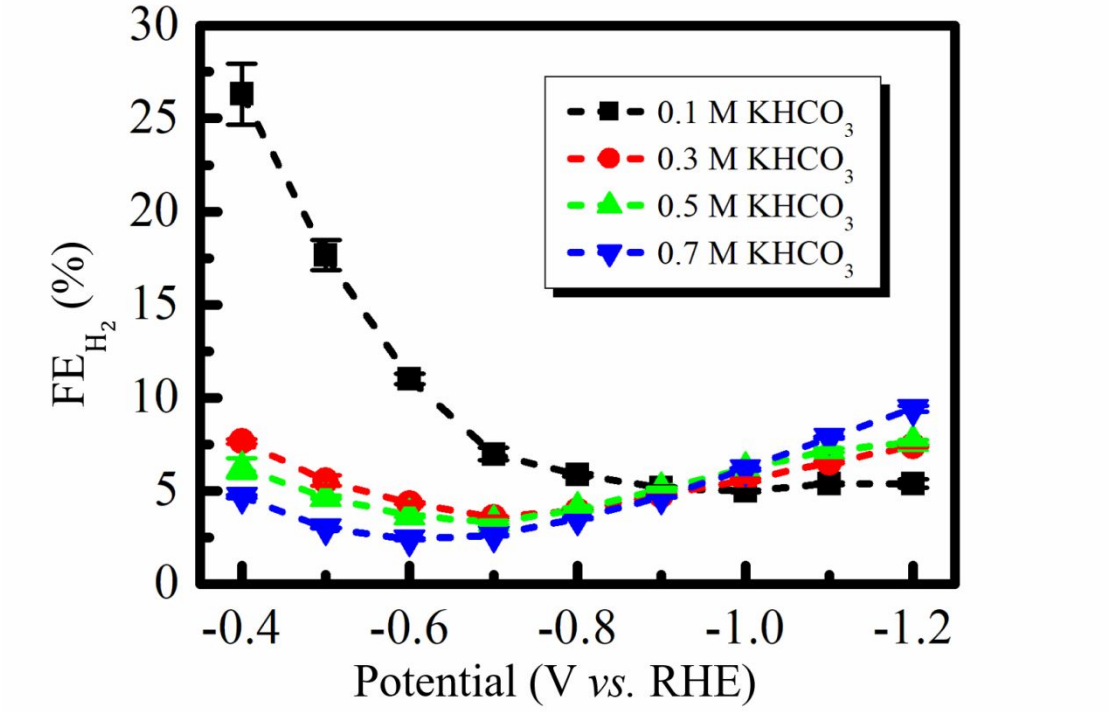

Figure S16. Faradaic efficiencies of H_2 at different potentials for Sn-OD-Cu in CO_2-saturated $KHCO_3$ solution with different concentrations

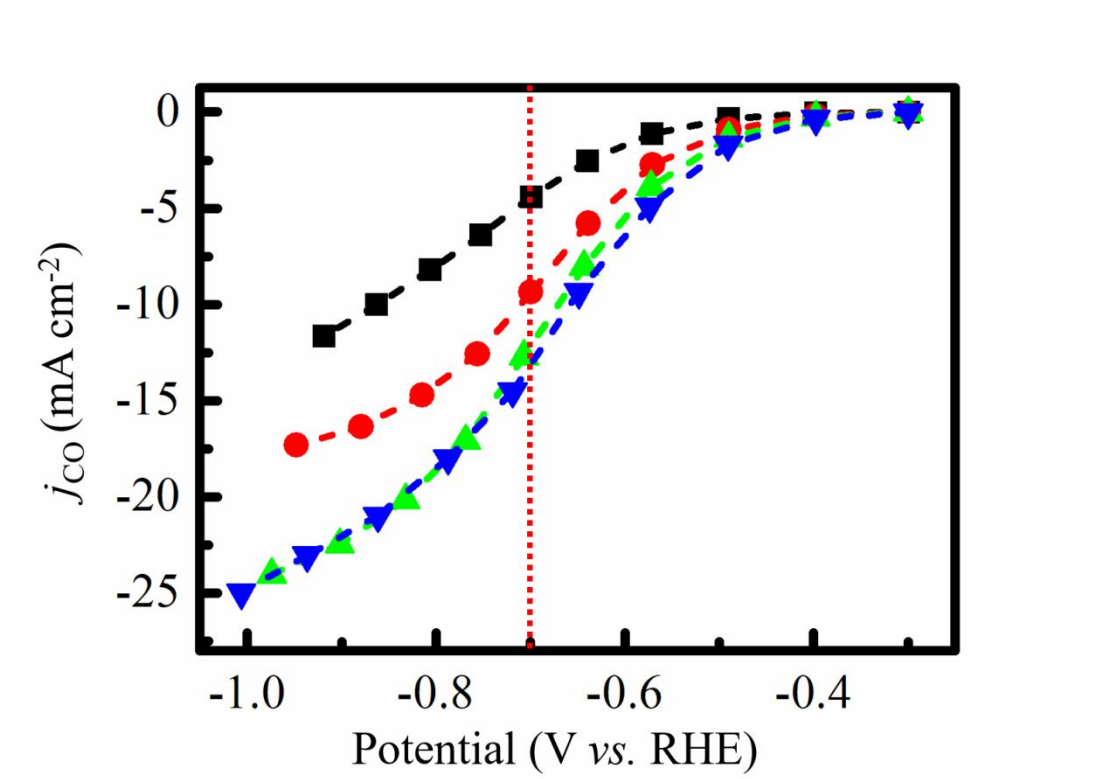

Figure S17. CO partial current densities of the Sn-OD-Cu in CO_2-saturated $KHCO_3$ solution with different concentrations at iR-corrected potentials.

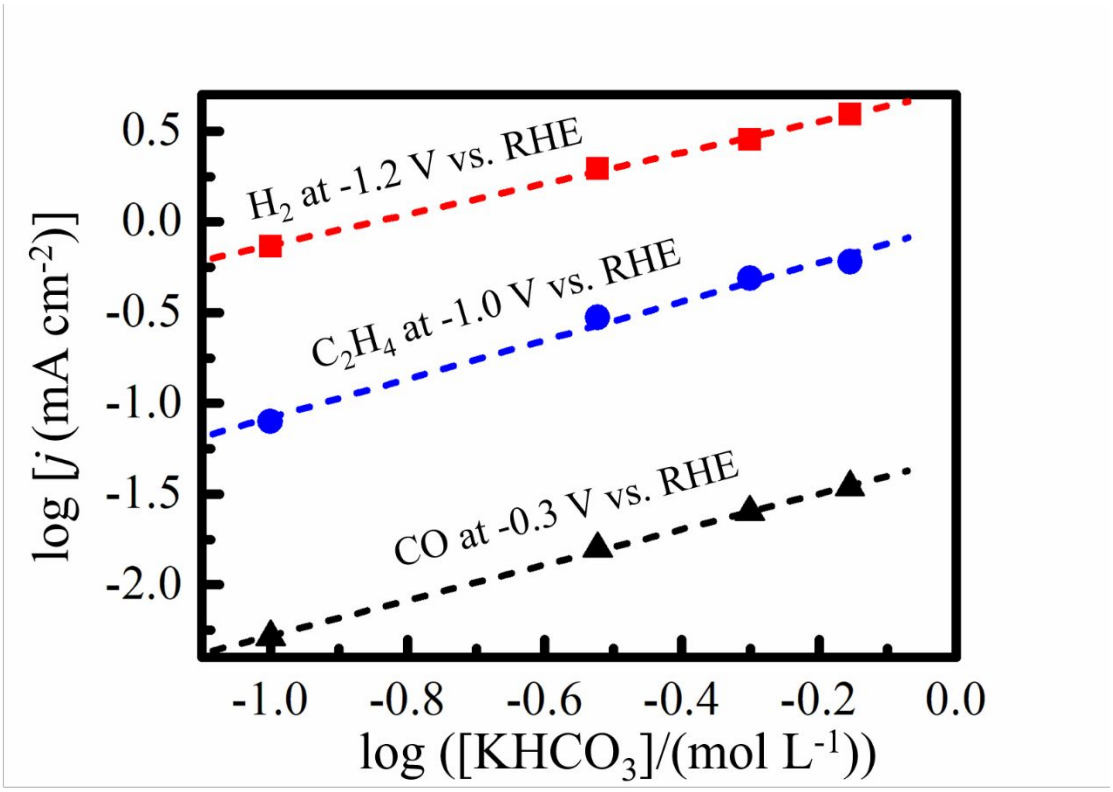

Figure S18. The partial current densities of the Sn-OD-Cu for CO, H_2, and C_2H_4 versus $KHCO_3$ concentration at constant potentials.

3. Supplementary Tables (Table S1–S4)

Table S1. Comparison of CO_2RR catalytic performance of Sn-OD-Cu with state-of-the-art noble metal-based catalysts in similar operating conditions.

Material	Electrolyte	E (V vs. RHE)	J (mA cm^{-2})	COFE (%)	COEE[b] (%)	Reference
Sn-OD-Cu	**0.1 M $KHCO_3$**	**-0.8**	**4.87**	**90.5**	**59.7**	**This work**
Sn-OD-Cu	**0.5 M $KHCO_3$**	**-0.7**	**8.5**	**94.6**	**65.7**	**This work**
Sn-OD-Cu	**0.7 M KHCO3**	**-0.6**	**5.01**	**98.1**	**71.8**	**This work**
Anodized Ag	0.1 M $KHCO_3$	-0.6	3.8	92.8	68.0	*Chem. Commun.*[21]
Silver Foam	0.1 M $KHCO_3$	-0.99	10.8	94.7	57.2	*ChemistrySelect.*[22]
Nanoporous Ag	0.5 M $KHCO_3$	-0.6	18	92	67.4	*Nat. Commun.*[23]
Nanocoral Ag	0.1 M $KHCO_3$	-0.6	6.6	95	74.4	*ACS Catal.*[24]
OD-Au	0.5 M $NaHCO_3$	-0.35	~2	96	81.4	*J. Am. Chem. Soc.*[25]
8 nm Au NPs	0.5 M $KHCO_3$	-0.67	~6.7[a]	90	63.5	*J. Am. Chem. Soc.*[26]
Au needles	0.5 M $KHCO_3$	-0.35	~15	95	80.6	*Nature.*[27]
2.4 nm Pd NPs	0.1 M $KHCO_3$	-0.89	~10	91.2	57.7	*J. Am. Chem. Soc.*[28]
3.7 nm Pd NPs	1 M $KHCO_3$	-0.7	-	93.4	64.9	*Nano Res.*[29]
Pd/C catalyst	0.1 M $KHCO_3$	-0.8	~4.2[c]	91.1	60.1	*Angew. Chem., Int. Ed.*[30]

[a] This value is not mentioned in the article but derived from the graphical results and calculated from

the current density and Faradaic efficiency. [b] These values are derived from the equations of S1 and S2. [c] The unit of current density is A g^{-1}. NPs, nanoparticles; COFE, Faradaic efficiency toward CO; COEE, energetic efficiency toward CO.

Table S2. R_u at different potentials in CO_2-saturated $KHCO_3$ solution with different concentrations.

Potential (V *vs.* RHE)	R_u (Ω)			
	0.1 M $KHCO_3$	0.3 M $KHCO_3$	0.5 M $KHCO_3$	0.7 M $KHCO_3$
-1.2	20.6	9.5	6.0	4.7
-1.1	20.5	9.7	6.2	4.8
-1.0	20.8	9.9	6.4	5.0
-0.9	20.9	10.0	6.5	5.1
-0.8	20.8	10.1	6.6	5.2
-0.7	21.0	10.1	6.7	5.3
-0.6	21.2	10.0	6.7	5.2
-0.5	21.1	10.0	6.6	5.2
-0.4	21.1	10.0	6.6	5.3
-0.3	21.5	10.1	6.7	5.4

Table S3. iR-corrected potentials in CO_2-saturated $KHCO_3$ solution with different concentrations.

Used potential (V *vs.* RHE)	iR-corrected potential (V *vs.* RHE)							
	0.1 M $KHCO_3$		0.3 M $KHCO_3$		0.5 M $KHCO_3$		0.7 M $KHCO_3$	
-1.2	-0.92	23.4%	-0.95	21.0%	-0.97	18.8%	-1.01	16.1%
-1.1	-0.86	21.6%	-0.88	20.1%	-0.90	18.0%	-0.94	14.9%
-1.0	-0.81	19.4%	-0.81	18.6%	-0.83	16.8%	-0.86	13.9%
-0.9	-0.75	16.4%	-0.76	16.0%	-0.77	14.7%	-0.79	12.5%
-0.8	-0.70	12.6%	-0.70	12.6%	-0.71	11.6%	-0.72	10.2%
-0.7	-0.64	8.7%	-0.64	8.8%	-0.64	8.1%	-0.65	7.3%
-0.6	-0.57	4.9%	-0.57	4.9%	-0.57	4.7%	-0.57	4.4%
-0.5	-0.49	2.0%	-0.49	2.0%	-0.49	1.9%	-0.49	1.9%
-0.4	-0.40	0.7%	-0.40	0.6%	-0.40	0.6%	-0.40	0.6%
-0.3	-0.30	0.3%	-0.30	0.1%	-0.30	0.1%	-0.30	0.1%

Table S4. The slopes of the plots of log (j_{CO} or j_{H2} or j_{C2H4}) versus log ([HCO_3^-]) at different potentials.

Potential (V *vs.* RHE)	Slopes of plots of log (*j*) *vs.* log ([HCO_3^-]) at different potentials		
	CO	H_2	C_2H_4
-1.2	0.41	0.85	1.36
-1.1	0.45	0.77	1.25
-1.0	0.51	0.7	1.07
-0.9	0.55	0.56	0.87
-0.8	0.62	0.37	0.83
-0.7	0.68	0.12	-
-0.6	0.76	-0.12	-
-0.5	0.84	-0.22	-
-0.4	0.94	-0.31	-
-0.3	0.98	-	-

4. References

(S1) Mavrikakis, M.; Hammer, B.; Nørskov, J. K. Effect of Strain on the Reactivity of Metal Surfaces. *Phys. Rev. Lett.* **1998,** *81*, 2819-2822.

(S2) Xin, H.; Vojvodic, A.; Voss, J.; Nørskov, J. K.; Abild-Pedersen, F. Effects of *d*-Band Shape on the Surface Reactivity of Transition-Metal Alloys. *Phys. Rev. B* **2014,** *89*, 115114.

(S3) Zhang, Y. Electronegativities of Elements in Valence States and Their Applications. 1. Electronegativities of Elements in Valence States. *Inorg. Chem.* **1982,** *21*, 3886-3889.

(S4) Takashima, T.; Suzuki, T.; Irie, H. Electrochemical Carbon Dioxide Reduction on Copper-Modified Palladium Nanoparticles Synthesized by Underpotential Deposition. *Electrochim. Acta* **2017,** *229*, 415-421.

(S5) Li, Q.; Fu, J.; Zhu, W.; Chen, Z.; Shen, B.; Wu, L.; Xi, Z.; Wang, T.; Lu, G.; Zhu, J. J.; Sun, S. Tuning Sn-Catalysis for Electrochemical Reduction of CO_2 to CO via the Core/Shell Cu/SnO_2 Structure. *J. Am. Chem. Soc.* **2017,** *139*, 4290-4293.

(S6) Zheng, X. L.; Ji, Y. F.; Tang, J.; Wang, J. Y.; Liu, B. F.; Steinruck, H. G.; Lim, K.; Li, Y. Z.; Toney, M. F.; Chan, K.; Cui, Y. Theory-Guided Sn/Cu Alloying for Efficient CO_2 Electroreduction at Low Overpotentials. *Nat. Catal.* **2019,** *2*, 55-61.

(S7) Peterson, A. A.; Abild-Pedersen, F.; Studt, F.; Rossmeisl, J.; Norskov, J. K. How Copper Catalyzes the Electroreduction of Carbon Dioxide into Hydrocarbon Fuels. *Energy Environ. Sci.* **2010,** *3*, 1311-1315.

(S8) Kepp, K. P. A Quantitative Scale of Oxophilicity and Thiophilicity. *Inorg. Chem.*

2016, *55*, 9461-9470.

(S9) Schwarz, H. A.; Dodson, R. W. Reduction Potentials of CO_2^- and the Alcohol Radicals. *J. Phys. Chem.* **1989,** *93*, 409-414.

(S10) Clark, E. L.; Ringe, S.; Tang, M.; Walton, A.; Hahn, C.; Jaramillo, T. F.; Chan, K.; Bell, A. T. Influence of Atomic Surface Structure on the Activity of Ag for the Electrochemical Reduction of CO_2 to CO. *ACS Catal.* **2019,** *9*, 4006-4014.

(S11) Rosen, J.; Hutchings, G. S.; Lu, Q.; Rivera, S.; Zhou, Y.; Vlachos, D. G.; Jiao, F. Mechanistic Insights into the Electrochemical Reduction of CO_2 to CO on Nanostructured Ag Surfaces. *ACS Catal.* **2015,** *5*, 4293-4299.

(S12) Hansen, H. A.; Varley, J. B.; Peterson, A. A.; Nørskov, J. K. Understanding Trends in the Electrocatalytic Activity of Metals and Enzymes for CO_2 Reduction to CO. *J. Phys. Chem. Lett.* **2013,** *4*, 388-392.

(S13) Dunwell, M.; Luc, W.; Yan, Y.; Jiao, F.; Xu, B. Understanding Surface-Mediated Electrochemical Reactions: CO_2 Reduction and Beyond. *ACS Catal.* **2018,** *8*, 8121-8129.

(S14) Ham, Y. S.; Choe, S.; Kim, M. J.; Lim, T.; Kim, S. K.; Kim, J. J. Electrodeposited Ag Catalysts for the Electrochemical Reduction of CO_2 to CO. *Appl. Catal., B* **2017,** *208*, 35-43.

(S15) Firet, N. J.; Smith, W. A. Probing the Reaction Mechanism of CO_2 Electroreduction over Ag Films via Operando Infrared Spectroscopy. *ACS Catal.* **2017,** *7*, 606-612.

(S16) Zhang, L.; Mao, F. X.; Zheng, L. R.; Wang, H. F.; Yang, X. H.; Yang, H. G.

Tuning Metal Catalyst with Metal-C_3N_4 Interaction for Efficient CO_2 Electroreduction. *ACS Catal.* **2018,** *8*, 11035-11041.

(S17) Gao, D.; Zhang, Y.; Zhou, Z.; Cai, F.; Zhao, X.; Huang, W.; Li, Y.; Zhu, J.; Liu, P.; Yang, F.; Wang, G.; Bao, X. Enhancing CO_2 Electroreduction with the Metal-Oxide Interface. *J. Am. Chem. Soc.* **2017,** *139*, 5652-5655.

(S18) Kim, K. S.; Kim, W. J.; Lim, H. K.; Lee, E. K.; Kim, H. Tuned Chemical Bonding Ability of Au at Grain Boundaries for Enhanced Electrochemical CO_2 Reduction. *ACS Catal.* **2016,** *6*, 4443-4448.

(S19) Zhu, W.; Zhang, Y. J.; Zhang, H.; Lv, H.; Li, Q.; Michalsky, R.; Peterson, A. A.; Sun, S. Active and Selective Conversion of CO_2 to CO on Ultrathin Au Nanowires. *J. Am. Chem. Soc.* **2014,** *136*, 16132-16135.

(S20) Liu, S.; Yang, H. B.; Huang, X.; Liu, L. H.; Cai, W. Z.; Gao, J. J.; Li, X. N.; Zhang, T.; Huang, Y. Q.; Liu, B. Identifying Active Sites of Nitrogen-Doped Carbon Materials for the CO_2 Reduction Reaction. *Adv. Funct. Mater.* **2018,** *28*, 1800499.

(S21) Zhou, L. Q.; Ling, C.; Jones, M.; Jia, H. Selective CO_2 Reduction on a Polycrystalline Ag Electrode Enhanced by Anodization Treatment. *Chem. Commun.* **2015,** *51*, 17704-17707.

(S22) Daiyan, R.; Lu, X.; Ng, Y. H.; Amal, R. Highly Selective Conversion of CO_2 to CO Achieved by a Three-Dimensional Porous Silver Electrocatalyst. *ChemistrySelect* **2017,** *2*, 879-884.

(S23) Lu, Q.; Rosen, J.; Zhou, Y.; Hutchings, G. S.; Kimmel, Y. C.; Chen, J. G.; Jiao, F. A Selective and Efficient Electrocatalyst for Carbon Dioxide Reduction. *Nat.*

Commun. **2014,** *5*, 3242.

(S24) Hsieh, Y.-C.; Senanayake, S. D.; Zhang, Y.; Xu, W.; Polyansky, D. E. Effect of Chloride Anions on the Synthesis and Enhanced Catalytic Activity of Silver Nanocoral Electrodes for CO_2 Electroreduction. *ACS Catal.* **2015,** *5*, 5349-5356.

(S25) Chen, Y.; Li, C. W.; Kanan, M. W. Aqueous CO_2 Reduction at Very Low Overpotential on Oxide-Derived Au Nanoparticles. *J. Am. Chem. Soc.* **2012,** *134*, 19969-19972.

(S26) Zhu, W.; Michalsky, R.; Metin, O.; Lv, H.; Guo, S.; Wright, C. J.; Sun, X.; Peterson, A. A.; Sun, S. Monodisperse Au Nanoparticles for Selective Electrocatalytic Reduction of CO_2 to CO. *J. Am. Chem. Soc.* **2013,** *135*, 16833-16836.

(S27) Liu, M.; Pang, Y.; Zhang, B.; De Luna, P.; Voznyy, O.; Xu, J.; Zheng, X.; Dinh, C. T.; Fan, F.; Cao, C.; de Arquer, F. P.; Safaei, T. S.; Mepham, A.; Klinkova, A.; Kumacheva, E.; Filleter, T.; Sinton, D.; Kelley, S. O.; Sargent, E. H. Enhanced Electrocatalytic CO_2 Reduction via Field-Induced Reagent Concentration. *Nature* **2016,** *537*, 382-386.

(S28) Gao, D.; Zhou, H.; Wang, J.; Miao, S.; Yang, F.; Wang, G.; Wang, J.; Bao, X. Size-Dependent Electrocatalytic Reduction of CO_2 over Pd Nanoparticles. *J. Am. Chem. Soc.* **2015,** *137*, 4288-4291.

(S29) Gao, D. F.; Zhou, H.; Cai, F.; Wang, D. N.; Hu, Y. F.; Jiang, B.; Cai, W. B.; Chen, X. Q.; Si, R.; Yang, F.; Miao, S.; Wang, J. G.; Wang, G. X.; Bao, X. H. Switchable CO_2 Electroreduction via Engineering Active Phases of Pd Nanoparticles. *Nano Res.* **2017,** *10*, 2181-2191.

(S30) Huang, H.; Jia, H.; Liu, Z.; Gao, P.; Zhao, J.; Luo, Z.; Yang, J.; Zeng, J. Understanding of Strain Effects in the Electrochemical Reduction of CO_2: Using Pd Nanostructures as an Ideal Platform. *Angew. Chem., Int. Ed.* **2017,** *56*, 3594-3598.